Chemical Engineering Journal 515 (2025) 163755

Contents lists available at ScienceDirect

Chemical Engineering Journal

journal homepage: www.elsevier.com/locate/cej

High-performance flexible molecular-based piezoelectric composites for wireless microelectronics

Yuying Wu [a,*], Xiao Pan [b], Xin Jin [c], Xianran Wang [e], Gang Zhou [d,*], Xinyuan Zhu [c], Youfu Wang [c,*]

[a] School of Electrical Engineering, Shanghai DianJi University, Shanghai 201306, PR China
[b] College of Materials, Shanghai Dianji University, Shanghai 201306, PR China
[c] School of Chemistry and Chemical Engineering, Frontiers Science Center for Transformative Molecules, Shanghai Jiao Tong University, Shanghai 200240, PR China
[d] Key Laboratory of Integrated Regulation and Resources Development on Shallow Lakes, Ministry of Education, College of Environment, Hohai University, Nanjing 210098, PR China
[e] State Key Laboratory of Featured Metal Materials and Life-cycle Safety for Composite Structures, School of Resources, Environment and Materials, Guangxi University, Nanning 530004, PR China

ARTICLE INFO

Keywords:
PEGs
Piezoelectric coefficients
Sensitivity
Ferroelectric semiconductor

ABSTRACT

Self-powered wireless sensing systems based on piezoelectric generators (PEGs) are widely applied in fields such as wearable devices, environmental monitoring, and intelligent transportation. This study aimed to enhance the piezoelectric coefficients (d_{33}) and sensitivity of flexible PEGs via incorporating a novel ferroelectric semiconductor $[C_9H_{21}N_2O]CuBr_4$ ($C_9H_{21}N_2O$, 4-Amino-2,2,6,6-tetramethylpiperidine-1-oxyl) into polymer PVDF, leading to the development of a groundbreaking ABC/PVDF composite for wireless microelectronics. By optimizing material properties, our system delivers superior mechanical-to-electrical conversion in capturing and interpreting human motion signals with high stability and accuracy. More surprisingly, the smart shoes can accurately monitor both running and walking, with step durations of 0.2 s and 0.8 s, respectively, which can track key data such as cadence, running speed, distance, and exercise time. Detailed analysises reveal that ACB/PVDF PEG exhibits large d_{33} of 60 pC/N, exceptional sensitivity of 120 mV kPa^{-1} and a rapid response time of 2.5 $\pm$ 0.1 ms. It is concluded that the large piezoelectric coefficients, improved conductivity of ACB/PVDF and stress-induced ferroelectric dipoles rearrangement and reorientation induced by abundant β-phase in PVDF result in its high-performence. This work uncovers the potential of integrating semiconductor property and piezoelectric effect, providing both theoretical and practical support for the development of new self-powered energy systems.

1. Introduction

Piezoelectric generators (PEGs), due to their ability to harvest mechanical energy from human activities, are considered a promising energy harvesting tool with advantages such as low power consumption, portability, and implantability [1]. They can be used for self-powered small electronic devices [2]. Various non-centrosymmetric materials, such as MoS_2, GaN, ZnO, and $BaTiO_3$, have been developed for the fabrication of PEGs [3–6]. Ferroelectrics, as piezoelectric materials with spontaneous polarization characteristics, play a significant role in the collection and conversion of energy signals. Their polarization and piezoelectric properties are widely applied in various smart devices, such as data storage, sensors, solar cells, and self-powered systems [7,8]. To generate energy under mechanical stress, the high polarization and non-centrosymmetric characteristics of materials are crucial.

In recent decades, organic–inorganic hybrid ferroelectric materials have emerged as a promising inorganic alternative, combining the advantages of organic molecules and inorganic groups at the molecular level. In addition to its unique optical and electronic properties, it is also highly valued for its structural tunability, mechanical flexibility, and low-temperature solution fabrication process [9–11]. Currently, organic–inorganic hybrid ferroelectric materials have made significant progress in the field of piezoelectricity. For example, Xiong *et al.* reported that the organic–inorganic hybrid ferroelectric crystal $(TMFM)_{0.26}(TMCM)_{0.74}CdCl_3$ exhibited a piezoelectric coefficient d_{33} of up to 1540 pC/N, approaching the level of commercial oxide materials

* Corresponding authors.
E-mail addresses: wyy2021h@163.com (Y. Wu), gangzhou@hhu.edu.cn (G. Zhou), wyfown@sjtu.edu.cn (Y. Wang).

https://doi.org/10.1016/j.cej.2025.163755
Received 26 February 2025; Received in revised form 3 May 2025; Accepted 12 May 2025
Available online 14 May 2025
1385-8947/

[12]. The ferroelectric material $(ATHP)_2PbBr_4$ (ATHP = 4-amino-tetrahydropyran) prepared by Xiong *et al.* shown a piezoelectric voltage coefficient g_{33} of up to 660.3 * 10^{-3} V m/N [13]. Later, Khan *et al.* found that the ferroelectric crystal $(ATHP)_2PbBr_2Cl_2$ has a piezoelectric coefficient d_{31} value of 64.2 pC/N, and a piezoelectric voltage coefficient g_{33} as high as 900 mV m/N [14]. However, most metal halide piezoelectric materials are typically brittle, have poor stability, and exhibit limited output performance. New applications for smart wearable devices, such as electronic skin, self-powered pacemakers and soft robots, requires a combination of piezoelectric performance, environmental stability, and mechanical flexibility. To better meet the needs of practical applications, extensive research has been conducted on ferroelectric composite films made from polymers (PDMS = polydimethylsiloxane, TPU = thermoplastic polyurethane) [15,16].

Different from the above common polymers, polyvinylidene fluoride (PVDF) has garnered widespread attention in applications such as sensors, energy harvesting devices, and flexible electronics due to its piezoelectric and ferroelectric properties. This material is not only highly processable into thin films but also demonstrates exceptional flexibility, enabling consistent performance retention across diverse geometries and maintaining structural integrity under cyclic mechanical stress. It is well known that PVDF has five different crystalline phases: α, β, γ, δ, and ε phases [17,18]. Among them, the β phase is notable for its unique molecular chain arrangement in a fully trans configuration (TTTT), which maximizes the molecular polarity. Additionally, PVDF offers exceptional corrosion resistance and chemical durability, enabling long-term stable operation in humid, acidic, alkaline, or corrosive environments with reliable performance. This overcomes the drawback of moisture sensitivity in organic–inorganic hybrid materials. Therefore, PVDF is highly compatible with modern flexible electronic device technology, making it an ideal material in this field. However, the electrical output performance of PEGs depends on several factors, such as the composition and structure of the polymer encapsulating material, electrode materials, and interface effects. Research has found that by incorporating semiconductor materials (such as graphene, carbon nanotubes, nanoparticles, *etc.*), the conductivity of PVDF can be significantly improved [19–21]. Additionally, increasing the content of the β phase enhances its electrical properties, thereby improving its performance in sensors, flexible electronics, and energy harvesting. Therefore, it can be inferred that when a semiconductor ferroelectric material is encapsulated in PVDF, its dual properties of both semiconductivity and ferroelectricity may not only reduce the electrode-material interfacial resistance but also enhance the β-phase content, thereby enhancing the piezoelectricity. This presents a significant advantage over insulating ferroelectrics in this field. Additionally, applying a certain force can induce the movement of ferroelectric domain walls, causing the reorientation or flipping of disordered domains, thereby enhancing the piezoelectric properties of materials. These aspects has received little attention in PEGs research.

Given that hybrid organic–inorganic ferroelectrics are rich, filling these particles into a PVDF flexible substrate to fabricate flexible integrated devices is a feasible approach. Considering environmental concerns, Cu-based organic–inorganic hybrid ferroelectric semiconductors have become an excellent alternative to lead-based ferroelectric materials, with a bandgap range of 1.43 to 2.5 eV [22,23]. Through the disorder–order phase transition of organic ligands or the induced distortion of inorganic polyhedral structures, these materials can exhibit excellent ferroelectric properties. Building on these insights, we introduce a novel copper-based halide ferroelectric semiconductor, $[C_9H_{21}N_2O]CuBr_4$, embedded in PVDF. This material exhibits remarkable multifunctional properties, including strong second harmonic generation (SHG) activity, a narrow optical bandgap (1.78 eV), and significant room-temperature ferroelectric polarization (2.9 μC cm^{-2}) at room temperature. By a simple blade-coating method, the $[C_9H_{21}N_2O]CuBr_4$ particles were embedded into PVDF. The composites with 8 wt% $[C_9H_{21}N_2O]CuBr_4$ filling (this film, referred to as ACB/PVDF, is used for subsequent testing) exhibit the optimal performance, such as large d_{33} of 60 pC/N. We evaluated the intrinsic ferroelectricity of ACB/PVDF through domain switching behavior, and revealed interesting domain changes under external forces. Ultimately, the self-powered sensor ACB/PVDF was constructed. It exhibited fast response, high sensitivity and stable output signals, enabling wireless transmission of piezoelectric signals. Since PEGs can be widely used in various fields, such as wearable devices, health monitoring, smart devices, *etc.* Thus, we precisely designed and it was successfully applied in human motion detection and smart shoes. This work paves the way for large-scale production of compatible, low-energy manufacturing energy harvesting devices and self-powered smart sensing systems (Fig. 1).

2. Results and Discussion

2.1. Crystal structure and ferroelectric semiconductor characteristics of $[C_9H_{21}N_2O]CuBr_4$

High-quality black crystal $[C_9H_{21}N_2O]CuBr_4$ was obtained through the room-temperature solution volatilization method (**Fig. S1**). Its single-crystal structure was analyzed using the Single Crystal X-ray Diffraction (SC-XRD) at room temperature. As shown in Fig. 1**a**, the structural analysis revealed that $[C_9H_{21}N_2O]CuBr_4$ crystallizes in the chiral monoclinic space group $P2_1$. The unit cell parameters are: a = 9.4439(9), b = 7.6035(7), c = 11.8988(12), α = γ = 90°, and β = 92.095° (**Table S1**). As a control group for comparison, we also prepared $[C_9H_{21}N_2O]CuCl_4$ crystal (**Fig. S1,2**). Since its structure is centrosymmetric, it is not the focus of this study. From the bond length analysis, it can be observed that the average Cu-Br bond length in $[C_9H_{21}N_2O]CuBr_4$ is 2.3897 Å, with a range of 2.3558(8) Å to 2.4202(8) Å. Similarly, the bond angle analysis reveals several different Br-Cu-Br angles, with an average of 110.16°, ranging from 98.72° to 131.75°. This indicates that Cu^{2+} is not at the center, and the polyhedron exhibits a clear tilted asymmetry, which is caused by the Jahn-Teller effect, leading to uneven electron distribution in the degenerate orbitals of the Cu^{2+} center [24]. The Raman spectroscopy of the $[C_9H_{21}N_2O]CuBr_4$ crystal in **Fig. S3** dispalys the peaks at 77 cm^{-1} and 172 cm^{-1}, corresponding to the deformation and bending of the Br-Cu-Br bond. A peak at 232.8 cm^{-1} was attributed to the asymmetric stretching of Cu-Br [25], which corresponds to the structure of tetrahedral distortion. The cation $[C_9H_{21}N_2O]^+$ is ordered, which results in the formation of a chiral center with an "R" configuration in $[C_9H_{21}N_2O]CuBr_4$ [26].

In order to preliminarily assess the thermal stability of the crystal, we detected thermogravimetric analysis (TGA) and differential scanning calorimetry (DSC). The TGA test showed that $[C_9H_{21}N_2O]CuBr_4$ exhibits

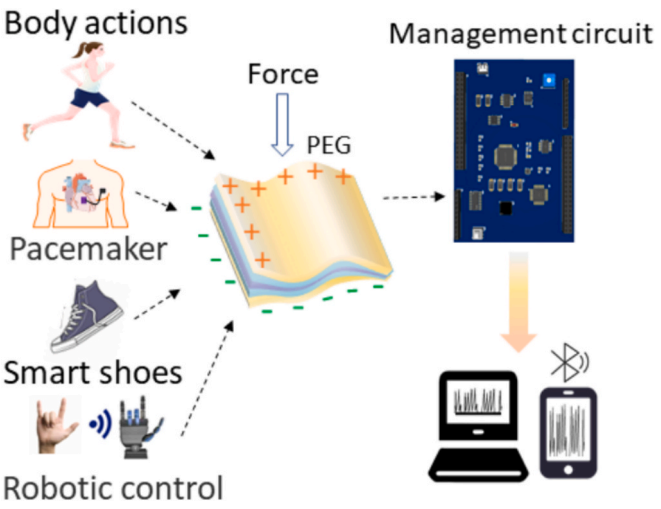

Fig. 1. Schematic of the PEGs for health monitoring and smart devices.

stability at temperatures well above room temperature, with a melting point at ~ 362 K. It then experienced a continuous weight loss of 21.7 % until 639.5 K (Fig. S4). Whatever, no phase transition peaks were observed in DSC. This is similar to previously reported [Cu(L-His)(bpy)] ClO_4·1.5H_2O crystal [27]. The scanning electron microscopy (SEM) and energy-dispersive X-ray spectroscopy (EDS) mapping of [$C_9H_{21}N_2O$]$CuBr_4$ show that the Cu and Br elements are evenly distributed (Fig. S5), and the quantitative analysis indicates an atomic ratio close to 1:4, which is consistent with the results from subsequent structural testing. To further verify the coordination environment of the Cu element in the crystal, we performed X-ray photoelectron spectroscopy (XPS) analysis. From the Cu 2*p* XPS spectrum shown in Fig. S6, it can be seen that the divalent copper is identified by the main peaks (Cu 2*p*1/2 and Cu 2*p*3/2) as well as the characteristic satellite peaks specific to Cu^{2+}. Additionally, we observed two weaker characteristic peaks for Cu^{+} at 951.7 eV and 931.9 eV, indicating that both Cu^{2+} and Cu^{+} are present in [$C_9H_{21}N_2O$]$CuBr_4$. The change in copper valence may be due to the defect in this crystal. To further analyze the strength of atomic interactions in the single crystal, dnorm-mapped Hirshfeld surfaces for the quantitative visualization of interactions in [$C_9H_{21}N_2O$]$CuBr_4$ was demonstrated. The 2D fingerprint plots were analyzed using the CrystalExplorer 3.1 program [28]. Red points on the dnorm-mapped Hirshfeld surface correspond to regions of strong interactions in Fig. 1**b**. It is clear that these strong interactions are hydrogen bonds between the hydrogen ions and halide ions. In [$C_9H_{21}N_2O$]$CuBr_4$, the main contribution of H···Br/Br···H interactions is 63.3 % (Fig. 1**d**), and the other interactions are shown in Fig. S7. In contrast, for [$C_9H_{21}N_2O$]$CuCl_4$, the contribution of H···Cl/Cl···H interactions is 58.2 % (Fig. S8). It is noteworthy that these 2D fingerprint plots are nearly mirror-symmetrical along the *de* = *di* partition line, which is attributed to the complementary Finside-Alloutside (Allinside-Foutside) contact pattern. In addition, calculations using the B3LYP/6-31G(d,p) basis set indicate that the stabilization energy of [$C_9H_{21}N_2O$]$CuBr_4$ is 4.82 kJ/mol, while that of [$C_9H_{21}N_2O$]$CuCl_4$ is 4.85 kJ/mol. Hydrogen bonding and ionic interactions exhibit strong long-range order, with stabilization energies in the range of 3–9 kJ/mol. Although van der Waals contacts account for most of the interactions in the crystal, they play a short-range role in molecules with relatively low stabilization energy (0.4–4 kJ/mol) [29]. Therefore, the hydrogen bonding and ionic interactions in the [$C_9H_{21}N_2O$]$CuBr_4$ structure demonstrate long-range order.

Due to the asymmetric chiral monoclinic space group $P2_1$ of the [$C_9H_{21}N_2O$]$CuBr_4$ structure, which belongs to a polar point group. Thus, the non-centrosymmetry of [$C_9H_{21}N_2O$]$CuBr_4$ was verified by investigating its nonlinear optical properties through second harmonic generation (SHG) [30]. Within the large wavelength range from 800 to 1064 nm, the SHG intensity increases progressively, reaching its maximum at 1040 nm (Fig. S9). Notably, the SHG intensity of [$C_9H_{21}N_2O$]$CuBr_4$ under this wavelength irradiation is nearly five times that of KH_2PO_4 (KDP) (Fig. S10), outperforming previously reported molecular ferroelectrics such as $(BA)_2(EA)_2Pb_3I_{10}$ (0.4 × KDP) [31], [2-FBA]$_2PbCl_4$ (0.9 × KDP) [32], and [(R/S)-3-aminopiperidine]PbI_4 (1 × KDP) [33]. In addition, the SHG intensity varies with angle, exhibiting a distinct bipolar behavior (Fig. 2**d**). Specifically, when the incident light polarization direction aligns with the its spontaneous polarization direction, the SHG intensity reaches its maximum. Conversely, when it is perpendicular, the SHG intensity is minimized. For variable temperature SHG test, the SHG signal gradually diminishes, ultimately dropping sharply beyond ~ 362 K (Fig. S11), which suggests a high melting point and a stable non-centrosymmetric structure. Since [$C_9H_{21}N_2O$]$CuBr_4$ belongs to a polar space group at room temperature, it is expected to exhibit ferroelectricity. To further verify the ferroelectric properties of [$C_9H_{21}N_2O$]$CuBr_4$ at room temperature, we conducted double-wave method measurements. The experiments yielded well-defined polarization–electric field (*P*-*E*) and current density–electric field (*J*-*E*) curves, confirming the ferroelectric nature of the crystal (Fig. 2**e**). In the ferroelectric loop, the polarization value (P_s) of [$C_9H_{21}N_2O$]$CuBr_4$ reaches 2.9 μC cm^{-2}, surpassing previously reported molecular ferroelectrics such as [Me_3NOH]$_2$[$KFe(CN)_6$] (1.25 μC cm^{-2}) [34], [$(CH_3)_2NH_2$]

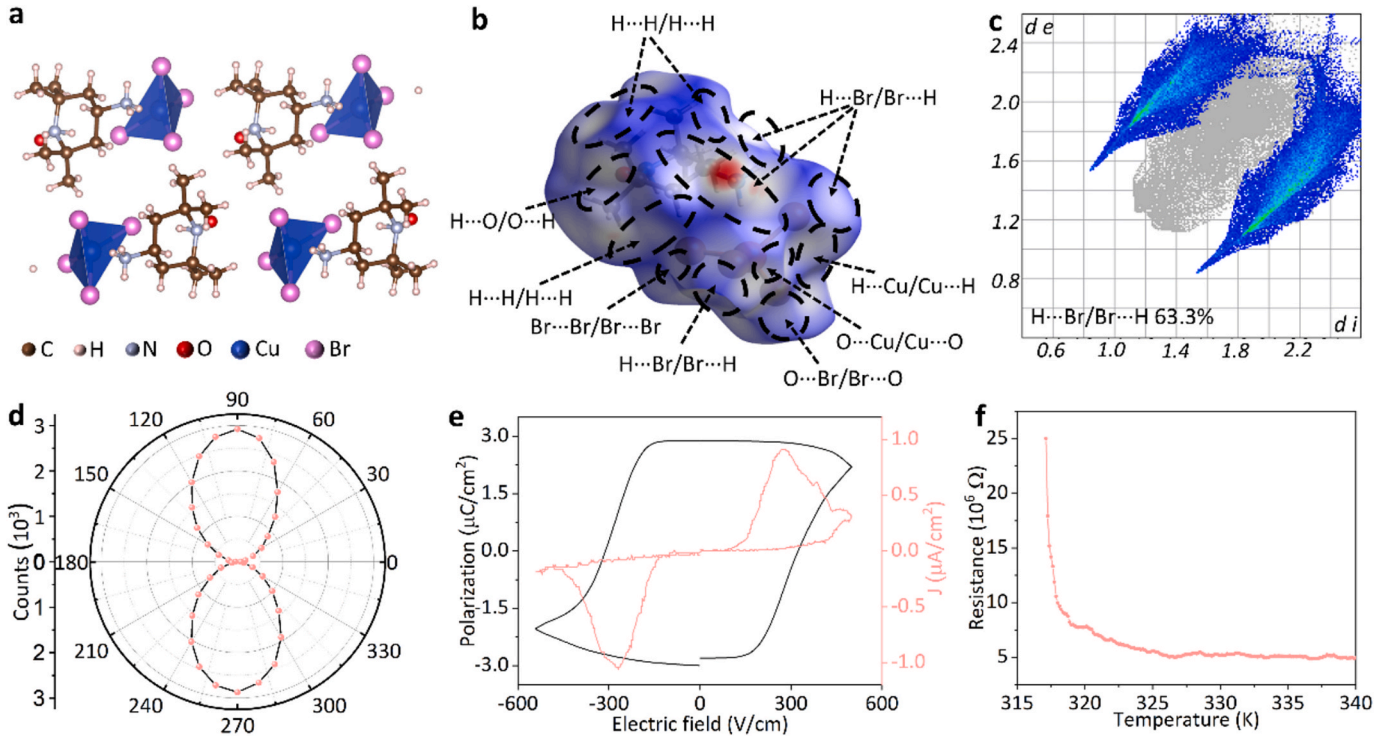

Fig. 2. (a) The crystal structure of [$C_9H_{21}N_2O$]$CuBr_4$. (b) Hirshfeld surface map and (c) two-dimensional fingerprint plot of the interactions in [$C_9H_{21}N_2O$]$CuBr_4$. (d) Polar plot of SHG anisotropy for [$C_9H_{21}N_2O$]$CuBr_4$ crystal. (e) Electric hysteresis loop and current curve of the [$C_9H_{21}N_2O$]$CuBr_4$ sample. (f) Temperature-dependent resistance of [$C_9H_{21}N_2O$]$CuBr_4$ crystal.

$[C_6H_5CH_2NH_2]_2BiBr_6$ (1 μC cm^{-2}) [35], and $(DMAA)CdCl_3$ (1.9 μC cm^{-2}) [36]. At room temperature, $[C_9H_{21}N_2O]CuBr_4$ demonstrates a coercive field strength (E_c) of 300 V cm^{-1} (0.3 kV cm^{-1}), considerably lower than that of high-performance ferroelectrics like $(3\text{-F-BTAB})PbBr_3$ with a small coercive field of 1.78 kV cm^{-1} [37]. A smaller coercive field means less electric field is needed to achieve polarization reversal.

For the sake of investigating the optical absorption property of this crystal, we tested the ultraviolet–visible absorption spectrum (**Fig. S12**). The band gap E_g of $[C_9H_{21}N_2O]CuBr_4$ was determined as 1.78 eV, which is smaller than some organic–inorganic hybrid ferroelectric semiconductors, including $(benzylammonium)_2PbCl_4$ (E_g = 3.65 eV) [38], $(C_4H_9NH_3)_2(NH_3CH_3)_2Sn_3Br_{10}$ (E_g = 2.22 eV) [39], and $[cyclohexylammonium]_2PbBr_4$ (E_g = 3.05 eV) [40]. To further demonstrate its semiconductor property, we tested the variation of resistance with temperature. As expected, the resistance of the crystal $[C_9H_{21}N_2O]CuBr_4$ gradually decreases as the temperature increases to 340 K (Fig. 2**f**), which reveals that the crystal exhibits semiconductor behavior. Thus, it is confirmed that the crystal is a ferroelectric semiconductor.

2.2. Structure and piezoelectric properties of flexible films.

From the above results, it is evident that $[C_9H_{21}N_2O]CuBr_4$ is a high-performance ferroelectric semiconductor. In order to obtain high conductivity and maintain excellent piezoelectric properties of piezoelectric device, we selected the organic polymer PVDF to fill with this ferroelectric semiconductor $[C_9H_{21}N_2O]CuBr_4$, and then studied its potential application. By dispersing the particles into the PVDF substrate, a flexible film was successfully fabricated (**Fig. S13**). In order to achieve the optimal performance ratio for the films, $[C_9H_{21}N_2O]CuBr_4$ crystal particles of 4 wt%, 6 wt%, 8 wt%, and 10 wt% were mixed with PVDF. These films exhibited excellent uniformity, integrity, and flexibility, with the thickness about 4 μm (Fig. 3**a**, **Fig. S14**). X-ray diffraction (XRD) and SEM measurements were performed (**Fig. S15**,**16**), and it was found that the film was smooth and the pure PVDF film exhibited the highest crystallinity. With the addition of $[C_9H_{21}N_2O]CuBr_4$ crystal, the high-quality crystallinity of the films was still maintained. To further investigate the effect of $[C_9H_{21}N_2O]CuBr_4$ on the phase transition of PVDF from the α phase to the β phase (TGTG to TTTT), Fourier-transform infrared (FTIR) spectroscopy was performed. From Fig. 3**b**, it can be seen that the spectrum primarily exhibits the obvious β phases, with characteristic peaks near 837 cm^{-1}, 1071 cm^{-1}, 1275 cm^{-1}, and 1410 cm^{-1} [41], while the α-phase at 975 cm^{-1} and 763 cm^{-1}. As the particle content increases, the intensity of the characteristic peaks corresponding to the β phase also increases, indicating that the crystallinity of the β phase in the films is enhanced. The β phase intensity reached its maximum when 8 wt% $[C_9H_{21}N_2O]CuBr_4$ was incorporated into the PVDF, forming the ACB/PVDF film (this film was used for subsequent tests). In order to know the β phase content, we calculated it basing on the equation derived from the Beer-Lambert law of absorbance:

$$F(\beta) = \frac{A_{837}}{\left(\frac{k_{837}}{k_{763}}\right)A_{763} + A_{837}}$$

Where the $F(\beta)$ is the β phase fraction, A_{763} and A_{837} are the characteristic peak intensities of α phase and β phase [27]. The k_{763} and k_{837} are the absorption coefficients, respectively. As shown in **Fig. S17**, $F(\beta)$ of PVDF is significant raised to 89 % for ACB/PVDF compare with that of PVDF film (69 %). Based on previous research, it is inferred that the coulomb interactions between the polar dipole groups of the microparticles promote the polar alignment of PVDF, thereby facilitating the formation of the β phase [42].

Since PVDF in the β phase is ferroelectric, and the $[C_9H_{21}N_2O]CuBr_4$ crystals themselves are ferroelectric, we used a double-wave method to measure the hysteresis loop of the ACB/PVDF films. As shown in Fig. 3**c**, the ACB/PVDF films exhibited standard polarization–electric field (P-E) curves and current density–electric field (J-E) curves. The remnant polarization (P_r) reaches a maximum value of 4.6 μC cm^{-2}, which is larger than the value of 1.267 μC cm^{-2} observed in P(VDF-TrFE) [43]. The E_c is ~70 kV/cm, which is smaller than that of pure PVDF [44], showing the

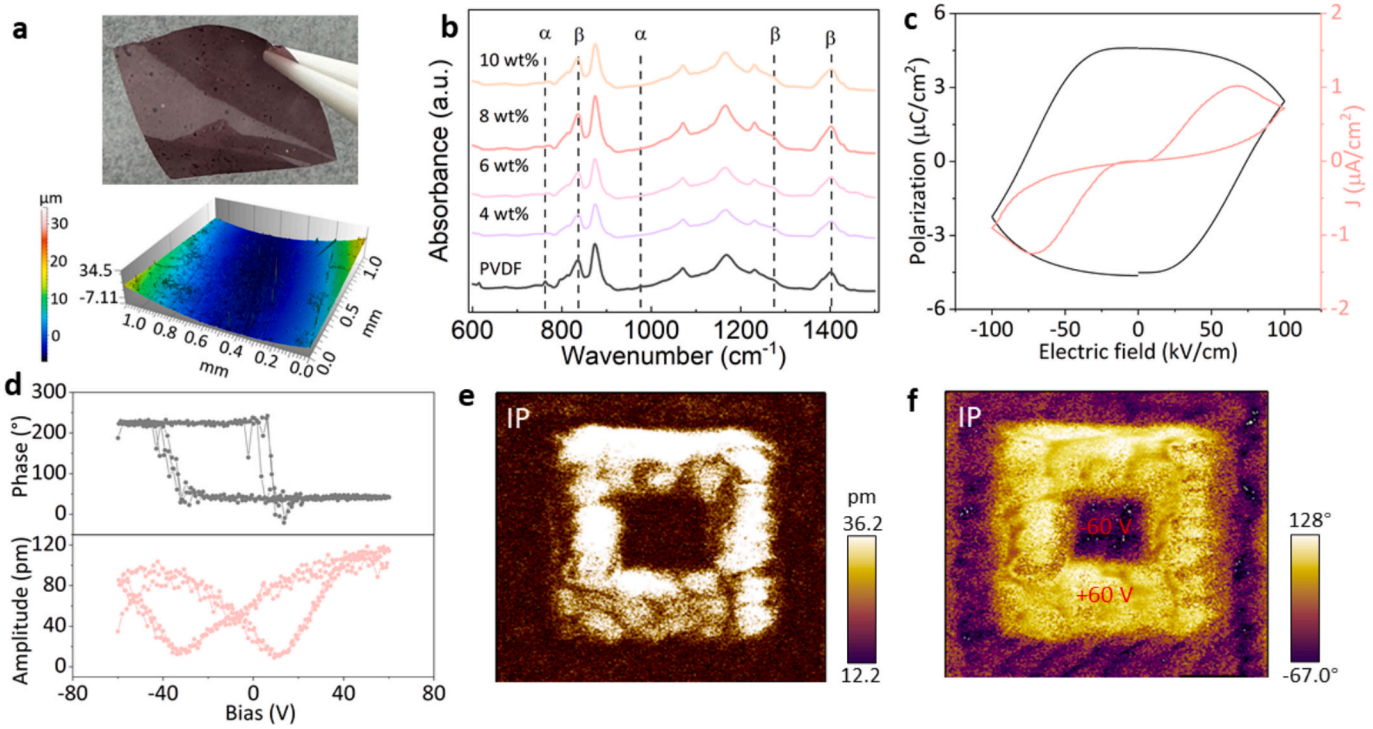

Fig. 3. (a) Optical image and white light confocal microscope scan of ACB/PVDF. (b) FTIR spectra of PVDF composite films with different contents of $[C_9H_{21}N_2O]CuBr_4$. (c) Macroscopic hysteresis loop and current curve of ACB/PVDF. (d) PFM switching hysteresis loops of phase and amplitude signals. (e) Amplitude and (f) phase maps of in-plane (IP) direction of selected area.

potential for use as a polarization switching. Thus, we are confident that the crystal filling increases the β phase, enhancing its ferroelectricity.

Furthermore, the Piezoelectric Force Microscopy (PFM) was used to investigate the local switching behavior of the ACB/PVDF films. In the 2 × 2 μm area, the multi-domain state of ACB/PVDF was observed (Fig. S18). Non-180° domain walls are clearly visible in the in-plane (IP, lateral) and out-of-plane (OP, vertical) phase images. Fig. S19 presents local PFM switching spectroscopy. The square phase-voltage hysteresis loops and butterfly-shaped amplitude-voltage loops indicating the switchable characteristics of ferroelectric domains in the ACB/PVDF thin films [45]. To further reveal the intrinsic ferroelectric of ACB/PVDF, we performed visual PFM domain switching behavior (Fig. 3**d-f**). First, a + 60 V voltage was applied to write into the central region of the multi-domain. Then, a −60 V voltage was applied to a smaller internal region. Subsequently, a box-in-box domain switching pattern was written onto the film sample (Fig. 3**e,f,** Fig. S20). The average phase difference between the positive and negative polarization regions matched the expected 180°, manifesting that the polarization is switchable and not caused by charge injection or electrostatic effects. As shown in Fig. 3**d**, the PFM amplitude hysteresis loop exhibited a butterfly shape, and the rectangular PFM phase signal switched by approximately 180°. These typical characteristics of ferroelectric polarization further validate the intrinsic ferroelectric behavior of ACB/PVDF, which is closely correlated with the high β-phase content in ACB/

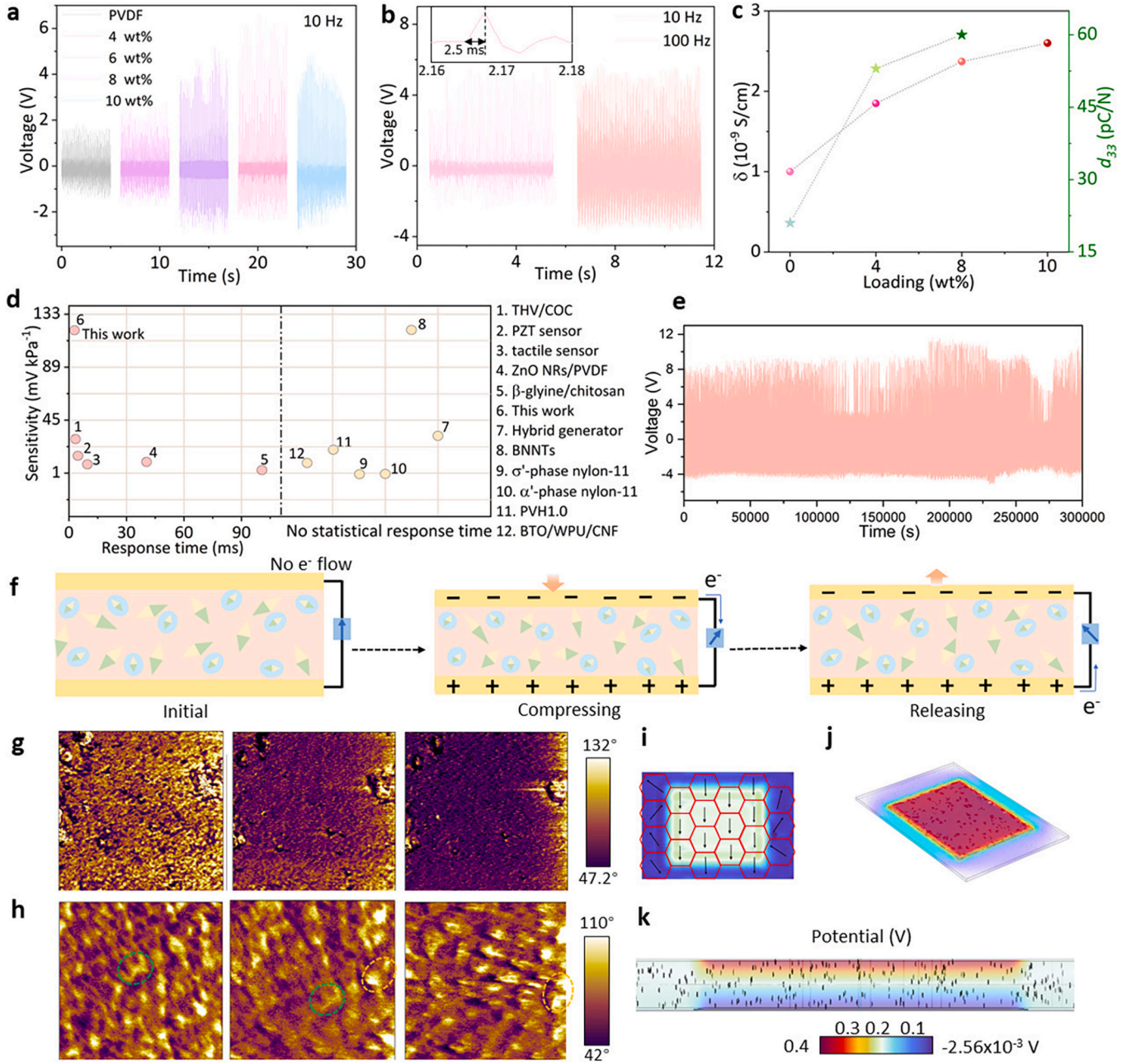

Fig. 4. (a) Output voltage of films with different $[C_9H_{21}N_2O]CuBr_4$ contents under 30 kPa and 10 Hz. (b) Output voltage of the ACB/PVDF PEG at 30 kPa under 10 Hz and 100 Hz. (c) The electrical conductivity and piezoelectric coefficients d_{33} of the films with different content $[C_9H_{21}N_2O]CuBr_4$. (d) Sensitivity comparison of flexible piezoelectric generators. (e) Output voltage of ACB/PVDF PEG at 30 kPa for mechanical stability testing. (f) Schematic of generating electric signal with stress and release conditions. (g) Changes of domain area in the phase map under mechanical forces of 21 nN, 37 nN, and 54 nN, respectively, where purple and yellow represent upward and downward ferroelectric domains, respectively. (h) Domain changes in the phase map under mechanical forces of 53 nN, 94 nN, and 128 nN, respectively. (i) Domain distribution simulation. (j) Deformation of composite film. (k) COMSOL simulations of the potential distribution of ACB/PVDF film.

PVDF film. During the PFM testing, the phase bias curve of ACB/PVDF exhibited significant asymmetry, which was also reflected in the amplitude curve. As mentioned earlier, such asymmetry in the local piezoelectric response is attributed to the presence of an internal electric field, which contributes to further enhancement of the piezoelectric performance [46].

2.3. Piezoelectric response of flexible ACB/PVDF

The large ferroelectric polarization and piezoelectric coefficient enable the material to generate stronger electrical signals under external stimuli (such as pressure or strain) [47]. To explore the piezoelectric response, a flexible ACB/PVDF PEG was prepared using a simple coating process. By adjusting the force magnitude and frequency, we carried out the periodic output voltage measurement of the ACB/PVDF PEG. Under a periodic pressure force 30 kPa at 10 Hz, a gradual increased voltage output was observed by the films with varying amounts of $[C_9H_{21}N_2O]CuBr_4$ (Fig. 4**a**). It is distinct that ACB/PVDF film with 8 wt% $[C_9H_{21}N_2O]CuBr_4$ exhibited the highest open-circuit voltage (V_{oc}) of 6.5 V, three times that of the pure PVDF film device. However, at 10 wt% doping, a noticeable decline in output voltage was observed. This decrease likely results from the higher concentration of $[C_9H_{21}N_2O]CuBr_4$ grains, which increases grain boundary resistance within the PVDF matrix. The electron accumulation at the grain boundaries, impeding electron movement and resulting in a decrease in voltage output [48]. The high-frequency stability of the ACB/PVDF at 100 Hz under 30 kPa pressure force was abtained in Fig. 4**b**. For the reasons of the highest piezoelectric response for ACB/PVDF, one is attributed to its large d_{33} up to 60 pC/N due to the highest β-phase content (Fig. 4**c,** **Fig. S21**). Second, the conductivity of ACB/PVDF increased due to the filling of semiconductor $[C_9H_{21}N_2O]CuBr_4$ (Fig. 4**c**). Third, the high polarization value of ACB/PVDF, which lead to a stronger internal polarized electric field during mechanical deformation, capturing more free charges [42]. Ultimately, charge capture ability enhanced and strengthened the piezoelectric response of the ACB/PVDF We also calculated the response time is 2.5 ± 0.1 ms and a sensitivity is 120 mV kPa^{-1} (**Fig. S22**), which surpasses that of other excellent piezoelectric generators (Fig. 4**d**) [27,49–57]. At 100 Hz, when the applied pressure was increased from 10 kPa to 30 kPa, the output voltage rose proportionally (**Fig. S23**). Moreover, ACB/PVDF PEG device maintained a stable output voltage for a long time (Fig. 4**e**), demonstrating its highly stable performance. Besides, it is apparent that the alternating positive and negative electric signals appear when pressed and withdrawn. As shown in Fig. 4**f,** this can be interpreted that when pressure is applied to ACB/PVDF, the dipoles align in response to the mechanical stress, resulting in a positive voltage output. Upon removing the force, the dipoles return to their original state or realign oppositely due to the elastic recovery of the piezoelectric materials. This release of the accumulated charge generates a reverse current, producing a negative voltage output.

As we know, the mechanical force can cause the dipoles within the domain to overcome the electrostatic force and align in the same direction, the spontaneous polarization is brought closer to the direction of the stress, forming stable ferroelectric domains that strengthen the piezoelectric response in that direction [58]. This phenomenon is commonly referred to as “stress-induced ferroelectric domain reorientation”. To investigate these microscopic changes of ferroelectric domains, we used PFM to study the domain switching of ACB/PVDF film at the microscale under different stresses. As shown in Fig. 4**g**, domain changes within the same region were observed under varying pressure levels of 21 nN, 37 nN, and 54 nN. At a force of 21 nN, alternating bright and dark domain structures in different directions appeared. When the pressure was increased to 37 nN, the domains became noticeably darker, indicating a significant shift in the orientation of the ferroelectric domains. When the pressure was further increased to 54 nN, the domain area became almost entirely dark, indicating that the electric dipole moment directions had nearly all aligned in the same direction. This phenomenon is similar to the ferroelectric domain behavior observed in $CuInP_2S_6$ (CIPS) films under applied force [59]. Thus, if the direction of the applied force does not initially align with the spontaneous polarization direction of the domains, the ferroelectric domains may tend to reorient, bringing the spontaneous polarization direction closer to the stress direction. This reorientation helps to lower the overall energy of ferroelectrics, creating a more stable polarization structure [60].

In addition, significant movement of domain walls occurs under pressure, especially under uniaxial or non-uniform pressure, where domain walls shift along the compression direction or the stress gradient. The movement happens because some domains increase in volume while others decrease. This shifting helps to rearrange the domain structure to align with the external pressure distribution. At a smaller scale, as illustrated in Fig. 4**h**, the ferroelectric domains within the highlighted circles exhibit noticeable shifts, accompanied by changes in the domain walls as pressure increases. The domain walls tend to migrate toward domains whose polarization direction aligns most closely with the direction of applied stress. When the pressure increased from 53 nN to 94 nN, the domains within the green circle visibly shifted, with the domains darkening due to dipole moment reversal, indicating domain wall disappearance. As the pressure further increased to 128 nN, the domains within the green circle vanished and merged with neighboring domains, resulting in a reversal of their polarization. The domains within the yellow circle expanded, accompanied by changes in domain walls. As pressure increased, the domain walls gradually bent or deflected. This bending helps the material form a more stable structure under local stress variations and reduces the extra energy caused by lattice distortion. During this process, the domain walls exhibit local bending or tilting, no longer retaining their original straight or flat alignment but instead adjusting to the surrounding stress distribution. Under cyclic external forces, domain wall movement induces larger displacement changes, resulting in an enhanced piezoelectric coefficient. This stress-induced domain reorientation mechanism plays a critical role in modulating piezoelectric performance. Additionally, Young’s modulus of ACB/PVDF (0.4 GPa), calculated from the PFM stress–strain curve tests (**Fig. S24**), further supports above adaptation. Combining the finite element simulation of the potential distribution in ACB/PVDF using COMSOL software, we vividly illustrated the reorientation of the dipole moment under external force (Fig. 4**i**). The simulation revealed that the stress distribution and the potential under pressure (Fig. 4**j,k**). It is thus clear that the simulation results are relatively closed to the experimental data.

2.4. Wireless transmission applications.

Based on the above research, we designed a piezoelectric generator system ACB/PVDF PEG for wearable human motion detection. The ACB/PVDF PEG, as the module in contact with the human body, converts analog signals into digital signals using an operational amplifier. These signals are then transmitted to the core unit, an STM32 microcontroller module, which processes and stores the sensor data. Subsequently, the data is sent to the host computer via a wireless transmission module, enabling signal detection during motion processes (Fig. 5**a**). To demonstrate the real-time detection of human signals by the ACB/PVDF sensor during running, we fixed the sensor to the finger, wrist, arm, and knee (Fig. 5**b**). By detecting changes in dynamic charge and corresponding output voltage, we recorded distinct electrical signals generated at different body parts. Our experiments revealed that in high-frequency, low-force scenarios like the finger and wrist, the ACB/PVDF PEG detected short-cycle, small-amplitude voltage signals (2–3 V). In contrast, in low-frequency, high-force scenarios like the arm and knee, the ACB/PVDF PEG exhibited long-cycle, large-amplitude voltage signals (4–5 V). These results clearly indicate that the ACB/PVDF PEG device can be used for monitoring various physiological activities and can adapt to a wide range of complex scenarios.

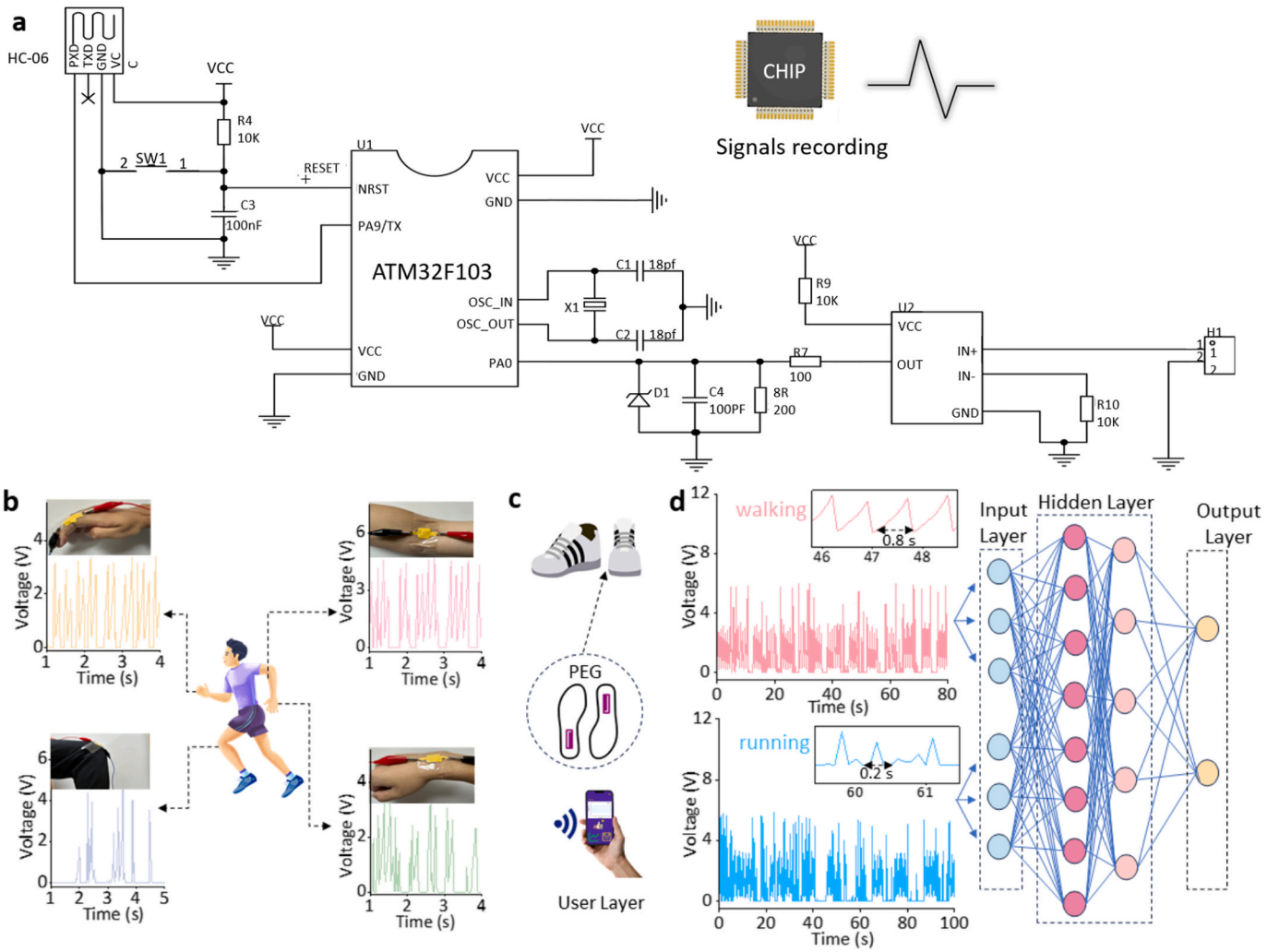

Fig. 5. (a) Circuit diagram and schematic of the device structure for the ACB/PVDF PEG. (b) Voltage signal detection from the fingers, wrist, arm, and knee. (c) Integration of ACB/PVDF PEG into the shoe sole. (d) Data analysis by combining ACB/PVDF PEG with machine learning models, providing intuitive feedback of information to users.

On the other hand, smart sports equipment will be a new development direction in the future. The ACB/PVDF PEG device can be embedded in the sole of shoes and connected wirelessly to a smartphone via bluetooth (Fig. 5**c**). The raw signals will be converted into feature vectors that can be processed by machine learning models. Methods such as Fourier transformation, time-domain analysis, or wavelet transform will be used to extract frequency and amplitude information from the signals. An appropriate model will be selected for training and validation, and the collected signals will be fed back to the user, achieving true intelligent device functionality. Fig. 5**d** shows that the voltage signal of the smart shoe system exhibits an approximately trapezoidal characteristic, with good repeatability and stability: when the sole hits the ground, an instantaneous positive voltage signal is generated; when the foot lifts off, the voltage rapidly decreases and eventually approaches zero. Thus, each step corresponds to a positive voltage signal, and the total step count can be calculated from the number of voltage peaks. The moving distance s and speed ν can be calculated using the formulas $s = n \times L$ and $\nu = L \times f$, where n, L and f represent total step count, step length and step frequency, respectively. Furthermore, exercise frequency is an important indicator to distinguish between walking and running. The voltage signal can be divided into two parts: red corresponds to walking, and blue corresponds to running (Fig. 5**d**). There is a difference in frequency between walking and running, with each step lasting approximately 0.8 ± 0.1 s for walking and 0.2 ± 0.1 s for running. It can enable health monitoring or remote monitoring. These novel human–machine interaction applications verify the excellent pressure-sensing performance. Hence, it is evident that the ACB/PVDF sensor we developed can play an important role in future healthcare and artificial intelligence applications.

3. Conclusion

In this study, we successfully designed and fabricated a self-powered piezoelectric generator, ACB/PVDF PEG, based on the ferroelectric semiconductor $[C_9H_{21}N_2O]CuBr_4$ and PVDF. The fabrication method is particularly simple, allowing for large-scale production. This PEG achieves efficient conversion of mechanical energy to electrical energy, demonstrating excellent output performance and stability. The ACB/PVDF PEG shows large piezoelectric coefficients of 60 pC/N, high conductivity and excellent mechano-electrical conversion capability compared to pure PVDF-based nanogenerators under a periodic pressure of 30 kPa. The open-circuit voltage is ~ 6.5 V, and a sensitivity is 120 mV kPa^{-1}. Cyclic testing manifested its durability. Through a deepgoing study of the ferroelectric domain evolution in ACB/PVDF under varying stress conditions, we elucidate the main mechanism by which stress-induced domain reorientation improves piezoelectric performance. Human motion detection and smart shoe applications demonstrate that this generator can continuously power low-power electronic devices,

showing great potential for use in wearable devices and smart sensing applications. In conclusion, this work provides valuable insights for the future development of electronic energy systems.

CRediT authorship contribution statement

Yuying Wu: Writing – review & editing, Writing – original draft, Validation, Project administration, Methodology, Investigation, Funding acquisition, Formal analysis, Data curation, Conceptualization. **Xiao Pan:** Writing – original draft, Methodology, Investigation. **Xin Jin:** Conceptualization. **Xianran Wang:** Investigation. **Gang Zhou:** Data curation, Conceptualization. **Xinyuan Zhu:** Project administration, Formal analysis. **Youfu Wang:** Validation, Methodology, Investigation.

Declaration of competing interest

The authors declare that they have no known competing financial interests or personal relationships that could have appeared to influence the work reported in this paper.

Acknowledgements

This work was supported by National Natural Science Foundation of China (12204301) and Shanghai RisingStar Program (Shanghai Sailing Program) (22YF1414300).

Appendix A. Supplementary data

Supplementary data to this article can be found online at https://doi.org/10.1016/j.cej.2025.163755.

Data availability

Data will be made available on request.

References

[1] F. Yang, J. Li, Y. Long, Z. Zhang, L. Wang, J. Sui, Y. Dong, Y. Wang, R. Taylor, D. Ni, W. Cai, P. Wang, T. Hacker, X. Wang, Wafer-scale heterostructured piezoelectric bio-organic thin films, *Science* 373 (6552) (2021) 337–342, https://doi.org/10.1126/science.abf2155.

[2] Z.-X. Huang, L.-W. Li, Y.-Z. Huang, W.-X. Rao, H.-W. Jiang, J. Wang, H.-H. Zhang, H.-Z. He, J.-P. Qu, Self-poled piezoelectric polymer composites via melt-state energy implantation, *Nat. Commun.* 15 (1) (2024), https://doi.org/10.1038/s41467-024-45184-4.

[3] J.K. Han, S. Kim, S. Jang, Y.R. Lim, S.-W. Kim, H. Chang, W. Song, S.S. Lee, J. Lim, K.-S. An, S. Myung, Tunable piezoelectric nanogenerators using flexoelectricity of well-ordered hollow 2D MoS2 shells arrays for energy harvesting, *Nano Energy* 61 (2019) 471–477, https://doi.org/10.1016/j.nanoen.2019.05.017.

[4] J. Cai, L. Yan, A. Seyedkanani, V. Orsat, A. Akbarzadeh, Nano-architected GaN metamaterials with notable topology-dependent enhancement of piezoelectric energy harvesting, *Nano Energy* 129 (2024) 109990, https://doi.org/10.1016/j.nanoen.2024.109990.

[5] J. Briscoe, E. Bilotti, S. Dunn, Measured efficiency of a ZnO nanostructured diode piezoelectric energy harvesting device, *Appl. Phys. Lett.* 101 (9) (2012) 093902, https://doi.org/10.1063/1.4749279.

[6] R. Peng, B. Zhang, G. Dong, Y. Wang, G. Yang, J. Zhang, B. Peng, Y. Zhao, M. Liu, Enhanced Piezoelectric Energy Harvester by Employing Freestanding Single-Crystal $BaTiO_3$ Films in PVDF-TrFE Based Composites, *Adv. Funct. Mater.* 34 (2024) 2316519, https://doi.org/10.1002/adfm.202316519.

[7] W. Li, C. Li, G. Zhang, L. Li, K. Huang, X. Gong, C. Zhang, A. Zheng, Y. Tang, Z. Wang, Q. Tong, W. Dong, S. Jiang, S. Zhang, Q. Wang, Molecular Ferroelectric-Based Flexible Sensors Exhibiting Supersensitivity and Multimodal Capability for Detection, *Adv. Mater.* 33 (44) (2021) 2104107, https://doi.org/10.1002/adma.202104107.

[8] Y. Zhang, X.-J. Song, Z.-X. Zhang, D.-W. Fu, R.-G. Xiong, Piezoelectric Energy Harvesting Based on Multiaxial Ferroelectrics by Precise Molecular Design, *Matter* 2 (3) (2020) 697–710, https://doi.org/10.1016/j.matt.2019.12.008.

[9] W. Li, Z. Wang, F. Deschler, S. Gao, R.H. Friend, A.K. Cheetham, Chemically diverse and multifunctional hybrid organic–inorganic perovskites, *Nat. Rev. Mater.* 2 (3) (2017) 16099, https://doi.org/10.1038/natrevmats.2016.99.

[10] G. Huang, C. Wang, H. Zhang, S. Xu, Q. Xu, Y. Cui, Post-healing of defects: an alternative way for passivation of carbon-based mesoscopic perovskite solar cells via hydrophobic ligand coordination, *J. Mater. Chem. A* 6 (6) (2018) 2449–2455, https://doi.org/10.1039/C7TA09646A.

[11] Y. Li, X. Zhang, H. Huang, S.V. Kershaw, A.L. Rogach, Advances in metal halide perovskite nanocrystals: Synthetic strategies, growth mechanisms, and optoelectronic applications, *Mater. Today* 32 (2020) 204–221, https://doi.org/10.1016/j.mattod.2019.06.007.

[12] W.-Q. Liao, D. Zhao, Y.-Y. Tang, Y. Zhang, P.-F. Li, P.-P. Shi, X.-G. Chen, Y.-M. You, R.-G. Xiong, A molecular perovskite solid solution with piezoelectricity stronger than lead zirconate titanate, *Science* 363 (6432) (2019) 1206–1210, https://doi.org/10.1126/science.aav3057.

[13] S. Deswal, S.K. Singh, P. Rambabu, P. Kulkarni, G. Vaitheeswaran, B. Praveenkumar, S. Ogale, R. Boomishankar, Flexible Composite Energy Harvesters from Ferroelectric A2MX4-Type Hybrid Halogenometallates, *Chem. Mater.* 31 (12) (2019) 4545–4552, https://doi.org/10.1021/acs.chemmater.9b01227.

[14] A.A. Khan, G. Huang, M.M. Rana, N. Mei, M. Biondi, S. Rassel, N. Tanguy, B. Sun, Z. Leonenko, N. Yan, C. Wang, S. Xu, D. Ban, Superior transverse piezoelectricity in organic-inorganic hybrid perovskite nanorods for mechanical energy harvesting, *Nano Energy* 86 (2021) 106039, https://doi.org/10.1016/j.nanoen.2021.106039.

[15] L.-C. An, C. Zhao, Y. Zhao, Y. Zhang, K. Li, A. Stroppa, W. Li, X.-H. Bu, Chiral 1D Hybrid Metal Halides with Piezoelectric Energy Harvesting and Sensing Properties, *Small Struct.* 4 (11) (2023) 2300135, https://doi.org/10.1002/sstr.202300135.

[16] S. Sahoo, T. Vijayakanth, P. Kothavade, P. Dixit, J.K. Zaręba, K. Shanmuganathan, R. Boomishankar, Ferroelectricity and Piezoelectric Energy Harvesting of Hybrid A2BX4-Type Halogenocuprates Stabilized by Phosphonium Cations, *ACS Mater. Au* 2 (2) (2022) 124–131, https://doi.org/10.1021/acsmaterialsau.1c00046.

[17] S. Wang, W. Tong, Y. Li, P. Zhang, Y. Liu, Y. Chen, Y. Zhang, Contributions of piezoelectricity and triboelectricity to a hydroxyapatite/PVDF–HFP fiber-film nanogenerator, Nano Energy 105 (2023) 108026, https://doi.org/10.1016/j.nanoen.2022.108026.

[18] J. Chen, C. Ayranci, T. Tang, Piezoelectric performance of electrospun PVDF and PVDF composite fibers: a review and machine learning-based analysis, *Mater. Today Chem.* 30 (2023) 101571, https://doi.org/10.1016/j.mtchem.2023.101571.

[19] J. Widakdo, Y.-H. Chiao, Y.-L. Lai, A.C. Imawan, F.-M. Wang, W.-S. Hung, Mechanism of a Self-Assembling Smart and Electrically Responsive PVDF–Graphene Membrane for Controlled Gas Separation, *ACS Appl. Mater. Interfaces* 12 (27) (2020) 30915–30924, https://doi.org/10.1021/acsami.0c04402.

[20] S. Wang, S. Liang, P. Liang, X. Zhang, J. Sun, S. Wu, X. Huang, In-situ combined dual-layer CNT/PVDF membrane for electrically-enhanced fouling resistance, *J. Membr. Sci.* 491 (2015) 37–44, https://doi.org/10.1016/j.memsci.2015.05.014.

[21] M. Sboui, W. Niu, G. Lu, K. Zhang, J.H. Pan, Electrically conductive TiO2/CB/PVDF membranes for synchronous cross-flow filtration and solar photoelectrocatalysis, *Chemosphere* 310 (2023) 136753, https://doi.org/10.1016/j.chemosphere.2022.136753.

[22] X.-L. Li, Z. Li, G. Zhang, G.-J. Yang; Lead-free perovskite $[H_3NC_6H_4NH_3]CuBr_4$ with both a bandgap of 1.43 eV and excellent stability. *J. Mater. Chem. A* 8(11) (2020) 5484-5488. Doi: 10.1039/C9TA12872G.

[23] P. Deschamps, P.P. Kulkarni, B. Sarkar, The Crystal Structure of a Novel Copper(II) Complex with Asymmetric Ligand Derived from l-Histidine, *Inorg. Chem.* 42 (23) (2003) 7366–7368, https://doi.org/10.1021/ic034760x.

[24] I. Živković, J.-R. Soh, O. Malanyuk, R. Yadav, F. Pisani, A.M. Tehrani, D. Tolj, J. Pasztorova, D. Hirai, Y. Wei, W. Zhang, C. Galdino, T. Yu, K. Ishii, A. Demuer, O. V. Yazyev, T. Schmitt, H.M. Rønnow, Dynamic Jahn-Teller effect in the strong spin-orbit coupling regime, *Nat. Commun.* 15 (1) (2024) 8587, https://doi.org/10.1038/s41467-024-52935-w.

[25] R. Mesbeh, B. Hamdi, R. Zouari, Crystal structure, thermal studies, Hirshfeld surface analysis, vibrational and DFT investigation of organic-inorganic hybrid compound $[C_9H_6NOBr_2]_2CuBr_4{\cdot}2H_2O$, *J. Mol. Struct.* 1125 (2016) 217–226, https://doi.org/10.1016/j.molstruc.2016.06.069.

[26] B.-B. Deng, C.-C. Xu, T.-T. Cheng, Y.-T. Yang, Y.-T. Hu, P. Wang, W.-H. He, M.-J. Yang, W.-Q. Liao, Homochiral Nickel Nitrite ABX_3 ($X = NO_2^-$) Perovskite Ferroelectrics, *J. Am. Chem. Soc.* 142 (15) (2020) 6946–6950, https://doi.org/10.1021/jacs.0c02580.

[27] R. Haldar, U. Sarkar, A. Kumar, D. Mandal, M. Shanmugam, Inducing Polar Phase in Poly(Vinylidene Fluoride) with a Molecular Ferroelectric Copper(II) Complex for Piezoelectric Energy Harvesting, *Adv. Funct. Mater.* 34 (46) (2024) 2407611, https://doi.org/10.1002/adfm.202407611.

[28] C.F. Mackenzie, P.R. Spackman, D. Jayatilaka, M.A. Spackman, CrystalExplorer model energies and energy frameworks: extension to metal coordination compounds, organic salts, solvates and open-shell systems, *IUCrJ* 4 (5) (2017) 575–587, https://doi.org/10.1107/S205225251700848X.

[29] Sriharsha V. Aradhya, Michael Frei, Mark S. Hybertsen, L. Venkataraman; Van der Waals interactions at metal/organic interfaces at the single-molecule level. *Nat. Mater.* 11(10) (2012) 872-876. Doi: 10.1038/nmat3403.

[30] K. Ding, H. Ye, C. Su, Y.-A. Xiong, G. Du, Y.-M. You, Z.-X. Zhang, S. Dong, Y. Zhang, D.-W. Fu, Superior ferroelectricity and nonlinear optical response in a hybrid germanium iodide hexagonal perovskite, *Nat. Commun.* 14 (1) (2023) 2863, https://doi.org/10.1038/s41467-023-38590-7.

[31] S. Han, X. Liu, Y. Liu, Z. Xu, Y. Li, M. Hong, J. Luo, Z. Sun, High-Temperature Antiferroelectric of Lead Iodide Hybrid Perovskites, *J. Am. Chem. Soc.* 141 (32) (2019) 12470–12474, https://doi.org/10.1021/jacs.9b05124.

[32] P.P. Shi, S.Q. Lu, X.J. Song, X.G. Chen, W.Q. Liao, P.F. Li, Y.Y. Tang, R.G. Xiong, Two-Dimensional Organic–Inorganic Perovskite Ferroelectric Semiconductors with Fluorinated Aromatic Spacers, *J. Am. Chem. Soc.* 141 (45) (2019) 18334–18340, https://doi.org/10.1021/jacs.9b10048.

[33] D. Fu, J. Xin, Y. He, S. Wu, X. Zhang, X.M. Zhang, J.H. Luo, Chirality-Dependent Second-Order Nonlinear Optical Effect in 1D Organic–Inorganic Hybrid Perovskite

Bulk Single Crystal, *Angew Chem. Int. Edit.* 60 (36) (2021) 20021–20026, https://doi.org/10.1002/anie.202108171.
[34] W.-J. Xu, P.-F. Li, Y.-Y. Tang, W.-X. Zhang, R.-G. Xiong, X.-M. Chen, A Molecular Perovskite with Switchable Coordination Bonds for High-Temperature Multiaxial Ferroelectrics, *J. Am. Chem. Soc*. 139 (18) (2017) 6369–6375, https://doi.org/10.1021/jacs.7b01334.
[35] B. Wang, D. Ma, H. Zhao, L. Long, L. Zheng, Room Temperature Lead-Free Multiaxial Inorganic-Organic Hybrid Ferroelectric, *Inorg. Chem*. 58 (20) (2019) 13953–13959, https://doi.org/10.1021/acs.inorgchem.9b01793.
[36] Z.-X. Wang, H. Zhang, F. Wang, H. Cheng, W.-H. He, Y.-H. Liu, X.-Q. Huang, P.-F. Li, Superior Transverse Piezoelectricity in a Halide Perovskite Molecular Ferroelectric Thin FilmC, *J. Am. Chem. Soc*. 142 (29) (2020) 12857–12864, https://doi.org/10.1021/jacs.0c06064.
[37] J.Y. Liu, M.M. Lun, Z.J. Wang, J.Y. Li, K. Ding, D.W. Fu, H.F. Lu, Y. Zhang, The H/F substitution strategy can achieve large spontaneous polarization in 1D hybrid perovskite ferroelectrics, *Chem. Sci.* 15 (40) (2024) 16612–16617, https://doi.org/10.1039/D4SC03571B.
[38] W.Q. Liao, Y. Zhang, C.L. Hu, J.G. Mao, H.Y. Ye, P.F. Li, R.G. Xiong, A lead-halide perovskite molecular ferroelectric semiconductor, *Nat. Commun*. 6 (1) (2015) 7338, https://doi.org/10.1038/ncomms8338.
[39] L. Li, X. Liu, C. He, S. Wang, C. Ji, X. Zhang, Z. Sun, S. Zhao, M. Hong, J. Luo, A Potential Sn-Based Hybrid Perovskite Ferroelectric Semiconductor, *J. Am. Chem. Soc*. 142 (3) (2020) 1159–1163, https://doi.org/10.1021/jacs.9b11341.
[40] Y.J. Cao, L. Zhou, L. He, P.P. Shi, Q. Ye, D.W. Fu, Phase Transition and Band Gap Regulation by Halogen Substituents on the Organic Cation in Organic–Inorganic Hybrid Perovskite Semiconductors, *Chem–eur J*. 26 (2020) 14124–14129, https://doi.org/10.1002/chem.202001266.
[41] Y. Yang, H. Sai, S.A. Egner, R. Qiu, L.C. Palmer, S.I. Stupp, Peptide programming of supramolecular vinylidene fluoride ferroelectric phases, *Nature* 634 (8035) (2024) 833–841, https://doi.org/10.1038/s41586-024-08041-4.
[42] J. Xia, H. Lu, G. Chen, D. Lin, W. Yang, C. Liu, B. Hu, Y. Zhao, High performance piezoelectric nanogenerator by fiber microstructure engineering toward self-powered wireless sensing system, *Nano Energy* 128 (2024) 109901, https://doi.org/10.1016/j.nanoen.2024.109901.
[43] R. Sahoo, S. Mishra, A. Ramadoss, S. Mohanty, S. Mahapatra, S.K. Nayak, An approach towards the fabrication of energy harvesting device using Ca-doped ZnO/PVDF-TrFE composite film, Polymer 205 (2020) 122869, https://doi.org/10.1016/j.polymer.2020.122869.
[44] C. Ribeiro, C.M. Costa, D.M. Correia, J. Nunes-Pereira, J. Oliveira, P. Martins, R. Gonçalves, V.F. Cardoso, S. Lanceros-Méndez, Electroactive poly(vinylidene fluoride)-based structures for advanced applications, *Nat. Protoc*. 46 (20) (2008) 2173–2187, https://doi.org/10.1002/polb.21550.
[45] Q. Gu, X. Lu, C. Chen, X. Wang, F. Kang, Y.Y. Li, Q. Xu, J. Lu, Y. Han, W. Qin, Q. Zhang, High-performance piezoelectric two-dimensional covalent organic frameworks, *Angew Chem. Int. Edit.* 63 (2024) e202409708, https://doi.org/10.1002/anie.202409708.
[46] J. Lin, F. Lv, Z. Hong, B. Liu, Y. Wu, Y. Huang, Ultrahigh Piezoelectric Response Obtained by Artificially Generating a Large Internal Bias Field in $BiFeO_3$–$BaTiO_3$ Lead-Free Ceramics, *Adv. Funct. Mater*. (2024) 2313879, https://doi.org/10.1002/adfm.202003619.
[47] S.S. Cheema, D. Kwon, N. Shanker, R. dos Reis, S.-L. Hsu, J. Xiao, H. Zhang, R. Wagner, A. Datar, M.R. McCarter, C.R. Serrao, A.K. Yadav, G. Karbasian, C.-H. Hsu, A.J. Tan, L.-C. Wang, V. Thakare, X. Zhang, A. Mehta, E. Karapetrova, R. V. Chopdekar, P. Shafer, E. Arenholz, C. Hu, R. Proksch, R. Ramesh, J. Ciston, S. Salahuddin, Enhanced ferroelectricity in ultrathin films grown directly on silicon, *Nature* 580 (7804) (2020) 478–482, https://doi.org/10.1038/s41586-020-2208-x.
[48] Y. Zhao, L.-C. An, K. Li, Y.-J. Gong, T.-M. Guo, F.-F. Gao, Y. Lei, Q. Li, W. Li, X.-H. Bu, A new piezoelectric hybrid metal thiocyanide for energy harvesting and human motion sensing, *Sci. China Mater*. 66 (5) (2023) 1854–1860, https://doi.org/10.1007/s40843-022-2360-x.
[49] W. Lin, B. Wang, G. Peng, Y. Shan, H. Hu, Z. Yang, Skin-Inspired Piezoelectric Tactile Sensor Array with Crosstalk-Free Row+Column Electrodes for Spatiotemporally Distinguishing Diverse Stimuli, *Adv. Sci*. 8 (3) (2021) 2002817, https://doi.org/10.1002/advs.202002817.
[50] W. Li, J. Duan, J. Zhong, N. Wu, S. Lin, Z. Xu, S. Chen, Y. Pan, L. Huang, B. Hu, J. Zhou, Flexible THV/COC Piezoelectret Nanogenerator for Wide-Range Pressure Sensing, *ACS Appl. Mater. Inter*. 10 (35) (2018) 29675–29683, https://doi.org/10.1021/acsami.8b11121.
[51] E.S. Hosseini, L. Manjakkal, D. Shakthivel, R. Dahiya, Glycine–Chitosan-Based Flexible Biodegradable Piezoelectric Pressure Sensor, *ACS Appl. Mater. Inter*. 12 (8) (2020) 9008–9016, https://doi.org/10.1021/acsami.9b21052.
[52] W. Feng, Y. Chen, W. Wang, D., Yu;A waterproof and breathable textile pressure sensor with high sensitivity based on PVDF/ZnO hierarchical structure, *Colloids Surface A* 633 (2022) 127890, https://doi.org/10.1016/j.colsurfa.2021.127890.
[53] L. Zhen, M. Cui, X. Bai, J. Jiang, X. Ma, M. Wang, J. Liu, B. Yang, Thin, flexible hybrid-structured piezoelectric sensor array with enhanced resolution and sensitivity, *Nano Energy* 131 (2024) 110188, https://doi.org/10.1016/j.nanoen.2024.110188.
[54] J. Liu, J. Liu, X. Zhang, X. Liu, C. Zhang, Customizing Three-Dimensional Elastic Barium Titanate Sponge for Intelligent Piezoelectric Sensing, *ACS Appl. Mater. Inter.*1 15 (2023) 52631–52640, https://doi.org/10.1021/acsami.3c12921.
[55] S. Naval, N.T. Beigh, D. Mukherjee, A. Jain, D. Mallick, Flexible V-shaped piezoelectric-triboelectric device for biomechanical energy harvesting and sensing, *J. Phys. D Appl. Phys*. 55 (2022) 365501, https://doi.org/10.1109/MEMS49605.2023.10052134.
[56] J. Zhang, S. Ye, H. Liu, X. Chen, X. Chen, B. Li, W. Tang, Q. Meng, P. Ding, H. Tian, X. Li, Y. Zhang, P. Xu, J. Shao, 3D printed piezoelectric BNNTs nanocomposites with tunable interface and microarchitectures for self-powered conformal sensors, *Nano Energy* 77 (2020) 105300, https://doi.org/10.1016/j.nanoen.2020.105300.
[57] S. Anwar, M. Hassanpour Amiri, S. Jiang, M.M. Abolhasani, P.R.F. Rocha, K. Asadi, Piezoelectric nylon-11 fibers for electronic textiles, energy harvesting and sensing, *Adv. Funct. Mater.* 31 (2021) 2004326, https://doi.org/10.1002/adfm.202004326.
[58] H. Fu, R.E. Cohen, Polarization rotation mechanism for ultrahigh electromechanical response in single-crystal piezoelectrics, *Nature* 403 (2000) 281–283, https://doi.org/10.1038/35002022.
[59] Y. Lun, X. Wang, J. Kang, Q. Ren, T. Wang, W. Han, Z. Gao, H. Huang, Y. Chen, L.-Q. Chen, D. Fang, J. Hong, Ultralow tip-force driven sizable-area domain manipulation through transverse flexoelectricity, *Adv. Mater.* 35 (2023) 2302320, https://doi.org/10.1002/adma.202302320.
[60] X. Yang, L. Han, H. Ning, S. Xu, B. Hao, Y.C. Li, T. Li, Y. Gao, S. Yan, Y. Li, C. Gu, W. Li, Z. Gu, Y. Lun, Y. Shi, J. Zhou, J. Hong, X. Wang, D. Wu, Y. Nie, Ultralow-pressure-driven polarization switching in ferroelectric membranes, *Nat. Commun.* 15 (1) (2024) 9281, https://doi.org/10.1038/s41467-024-53436-6.